Soft Matter

COMMUNICATION

Cite this: *Soft Matter*, 2019, **15**, 3283

Received 15th November 2018, Accepted 22nd March 2019

DOI: 10.1039/c8sm02338g

rsc.li/soft-matter-journal

Indication of a twist-grain-boundary-twist-bend phase of flexible core bent-shape chiral dimers†

Matthew T. Murachver,[a] Ahlam Nemati,[a] Mirosław Salamończyk, ‡[ab] Carson Bullock,[ac] Zachary Sabata,[ade] Haumed Rahmani,[a] Tetiana Vorobiova,[a] Alain Izadnegahdar,[f] Seyyed Muhammad Salili,[ag] Victoria Norman, [b] Chenhui Zhu,[b] Torsten Hegmann, [ah] Samuel N. Sprunt,[i] James T. Gleeson[i] and Antal I. Jakli *[ai]

The effect of the molecular chirality of chiral additives on the nanostructure of the twist-bend nematic (N_{TB}) liquid crystal phase with ambidextrous chirality and nanoscale pitch due to spontaneous symmetry breaking is studied. It is found that the ambidextrous nanoscale pitch of the N_{TB} phase increases by 50% due to 3% chiral additive, and the chiral transfer among the biphenyl groups disappears in the N_{TB}* phase. Most significantly, a twist-grain boundary (TGB) type phase is found at $c > 1.5$ wt% chiral additive concentrations below the usual N* phase and above the non-CD active N_{TB}* phase. In such a TGB type phase, the adjacent blocks of pseudo-layers of the nanoscale pitch rotate across the grain boundaries.

A. Introduction

Chiral liquid crystals (LCs) from rod-shaped molecules present various examples of molecular chirality, where either the chiral center is built into the mesogenic molecules or chiral compounds are dissolved as 'guests' in achiral LC 'hosts'. In bent-core liquid crystal (BCLC) materials, structural chirality occurs mainly *via* spontaneous chiral symmetry breaking. Experimental examples for such structures include tilted polar smectic phases,[1–3] the dark conglomerate phase[4,5] and the helical nanofilament (HNF) phase[6–9] of BCLCs.

Bent-core molecules may also form a twist-bend nematic (N_{TB}) phase, whereby bent-shaped molecules have a heliconical director structure.[10] Experimentally the N_{TB} phase was observed first in flexible BCLC dimers, where two rigid arms are connected by methylene or ether linkages with an odd number of carbons.[11–19] Analysis of flexoelectric measurements[18] and freeze-fracture transmission electron microscopy (FF-TEM) studies proved that the heliconical pitch is in the 10 nm range,[17,20] which is much smaller than the smallest pitch ever observed (>0.1 μm) for chiral nematic materials.[21]

Chiral flexible dimers were reported to have a sequence of up to seven distinct nematic phases with the highest-temperature mesophase being either the cholesteric (N*) or one of the blue phases.[22,23] The stable phases observed at lower temperatures are variants of the N_{TB} phase with apparently much larger pitch than that in the achiral N_{TB} dimers, and the lowest temperature phase seems to expel the chiral twist and develop a bent-splay modulation.[22,23]

Chirality of flexible bent-shape dimers can also be achieved by chiral molecular additives.[24–26] In the nematic phase of these mixtures, a helical structure forms that resemble a normal N* phase. The main difference is the spontaneous formation of various stripe textures[27] that can be understood as a consequence of the bend elastic constant K_{33} being smaller than the twist elastic constant K_{22}.[17,28] Additionally, above a certain electric or magnetic field threshold, a "heliconical" state may form, where the helical axis makes an angle $\theta < 90^\circ$ with the director. Such a state was already theoretically predicted almost 50 years ago by Meyer[29] and de Gennes[30] for N* materials with $K_{33} < K_{22}$. Experimentally the pitch of the heliconical structure was found to be electrically[31–33] and magnetically[34] tuneable from the UV to infrared range.

The effect of the chiral additive on the structure of the N_{TB} phase has a significance arching over the liquid crystal science, since it represents an interaction between the molecular chirality and spontaneous chiral symmetry breaking with ambidextrous nanoscale chirality. It has been studied theoretically,[35] and experimental observations have shown that the helical pitch becomes distorted,[24] or is even expelled,[25] in the chiral N_{TB}

[a] *Chemical Physics Interdisciplinary Program & Liquid Crystal Institute, Kent State University, Kent, OH 44242, USA. E-mail: ajakli@kent.edu*
[b] *Advanced Light Source, Lawrence Berkeley National Laboratory, Berkeley, California 94720, USA*
[c] *Department of Physics, College of Wooster, Wooster, OH 44691, USA*
[d] *Department of Physics, University of Nebraska, Omaha, NE 68182, USA*
[e] *Department of Chemistry, University of Nebraska, Omaha, NE 68182, USA*
[f] *Advanced Precision Systems, Inc., Chagrin Falls, OH, USA*
[g] *Department of Physics & Astronomy, University of Pennsylvania, Philadelphia, USA*
[h] *Department of Chemistry and Biochemistry, Kent State University, Kent, OH 44242, USA*
[i] *Department of Physics, Kent State University, Kent, OH 44242, USA*
† Electronic supplementary information (ESI) available. See DOI: 10.1039/c8sm02338g
‡ Current address: University of Warsaw, Faculty of Chemistry, Żwirki i Wigury 101, 02-089 Warszawa, Poland.

(N_{TB}*) phase. Recently, the existence of a novel N_X phase was reported below the N_{TB} phase when a chiral additive with very high helical twisting power was used.[36] However, no quantitative results are known about the effect of the chiral additives on the ambidextrous nanoscale pitch formed by spontaneous symmetry breaking.

Using resonant soft X-ray (RSoXS),[15,16] induced circular dichroism (iCD) and several optical microscopy experimental techniques, here we report the first quantitative results on the effect of chiral additives on the nanostructure and chiral transformation of a mixture of achiral LC dimers with the room temperature N_{TB} phase. We found up to 50% increase in the nanoscale pitch below 3 wt% chiral additive concentration, which is opposite to the decrease of the micron-scale pitch with increasing chiral additive concentration (c) in the N* phase. Additionally, for $c \geq 1.5$ wt% chiral additive concentrations, we found a new phase between the N* and N_{TB}* phases, which resembles the twist-grain-boundary (TGB) phase of the chiral smectics and we designate this phase as TGB_{TB}.

B. Materials and methods

We investigated the LC mixture KA(0.2) with a chiral additive ZLI811. Both materials were obtained from Merck and used without further purification. KA(0.2) (see molecular structures in Fig. S1 in ESI†) is a combination of a five-component mixture of ether-linked fluorinated biphenyls[28] and 20 mol% of the methylene linked dimer compound 1″,9″-bis(4-cyano-2′-fluorobiphenyl-4′-yl)nonane (CBF9CBF).[28] Pure KA(0.2) exhibits an I – 75.0 °C – N – 37.5 °C – N_{TB} phase sequence. ZLI811 has an S-configuration with helical twisting power of about 10 μm^{-1}, and is known to promote a single left-handed cholesteric phase in typical calamitic mesogens. We added ZLI811 to KA(0.2) at 0.5, 1, 1.5, 2.0, 2.5, 3, and 3.5% concentrations by weight.

The temperature-dependent polarized optical microscopy (POM) studies were carried out using an Olympus BX60 equipped with an Instec HS200 heat stage. The temperature dependence of the optical birefringence and the distribution of the optic axis were monitored by the Phi-Viz Imaging System from Polaviz (APSYS Inc.) that combines 3-variable LC-based devices with POM Olympus BX51, a Polaviz Heater and Polaviz Temperature Controller.

For the optical studies, films with thicknesses ranging from 4 μm to 10 μm were used. The inner surfaces of the transparent indium tin oxide (ITO) coated glass substrates were treated with a unidirectional rubbed polyimide PI2555 (HD Micro Systems) that promotes molecular alignment parallel to the substrates (planar alignment) and along the rubbing direction. Studies of films with planar alignment were supplemented with microscopy on homeotropic aligned cells with inner surfaces coated with PI 1211 and plano-wedge cells assembled with a 5 cm radius convex lens and planar glass with inner surfaces of rubbed polyvinyl alcohol (PVA) promoting planar alignment.

The UV-vis absorption spectrum was measured with a Shimatzu UV-3600 Plus spectrophotometer, and iCD spectropolarimetry was carried out by an OLIS DSM 17 (http://olisweb.com). The iCD measurements were carried out on 7 μm films of KA(0.2) doped by c = 0–3.5 wt% ZLI811 sandwiched between untreated quartz glass plates. The birefringence was cancelled by averaging 8 signals measured after 45° consecutive rotations of the sample. Details of the iCD experiments are given in ref. 37.

C. Experimental results

Since the N–N_{TB} transition of KA(0.2) is almost second order,[28] the DSC measurements proved to be sensitive only to the isotropic–N or N* phase transitions, and showed a monotonous decrease of the I–N(N*) transition from 75 °C for neat KA(0.2) to 69 °C for KA(0.2) + 3% ZLI811 (see Fig. S2, ESI†). To determine the phase transitions on cooling from the N* phase, we combined the results of optical detections (POM and Phi-Viz Imaging), RSoXS and CD measurements. The results of those measurements are presented in Fig. 1–5 and Fig. S3–S5 (ESI†).

The POM textures of a 10 μm KA(0.2)* film at selected temperatures under 1 °C min^{-1} cooling rate with the chiral additive concentration varying horizontally are shown in Fig. 1. The concentration gradient in the contact preparation cells of Fig. 1 is achieved by inserting the pure parent liquid crystal at one side of the empty cell with constant thickness d and the liquid crystal with fixed chiral dopant concentration c from the opposite side. After the fluids meet at the center, the material is heated to the isotropic phase, allowing partial diffusion of the chiral material. In this case, a series of bands appear as seen in Fig. 1. Fig. 1(a) shows the sample at 35.5 °C, when the material is in the N* phase showing 7 bands with different colours

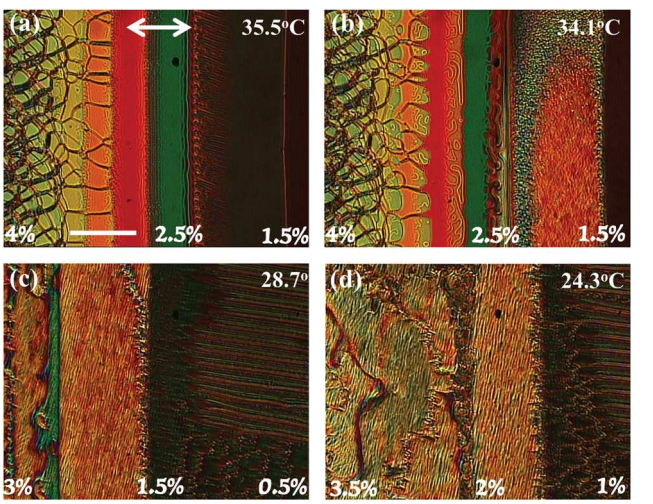

Fig. 1 The POM textures of a 10 μm thick cell with contact preparation of KA(0.2) and chiral additive ZLI811 at different temperatures, with increasing additive concentrations from right to left in each image. (a) At 35.5 °C in the N* phase; (b) at 34.1 °C where the mixture for ~1.5% ZLI811 transitions to another phase; (c) at 28.7 °C where above 2.5% ZLI811 the mixture transitions to another phase; (d) at 24.3 °C where the texture below 1.5% ZLI811 is consistent with the N_{TB} phase (stripes parallel to rubbing direction) and the texture above 1.5% ZLI811 indicates another phase (stripes normal to the rubbing direction). The white double arrow corresponds to the direction of surface rubbing, and the white scale bar indicates 100 μm length. Polarizers and analyzers are parallel to the edges of the pictures.

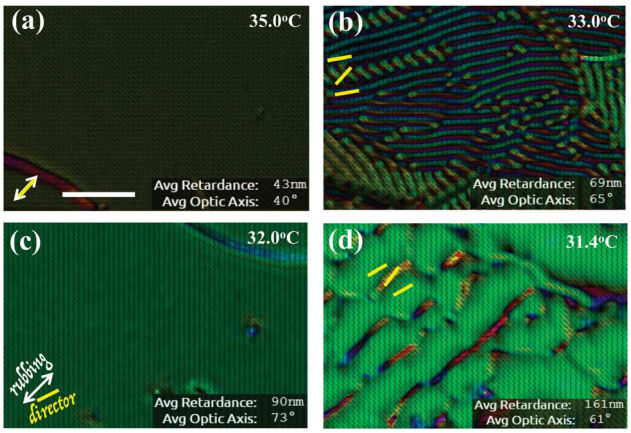

Fig. 2 Phi-Viz images for a L = 4.7 μm film of KA(0.2) + 2% ZLI811 at various temperatures. The dark lines are perpendicular to the LC director. (a) 35.0 °C, uniform texture in the N* phase; (b) 33.0 °C, stripe domains with different orientations; (c) 32.0 °C, texture with uniform director with direction making 33° with the rubbing direction; (d) 31.4 °C texture with the stripes forming along the rubbing direction resembling the optical stripes typical of the N_{TB} phase. White bar shows 50 μm length. Insets at the bottom-right show the average retardance and average optical axis.

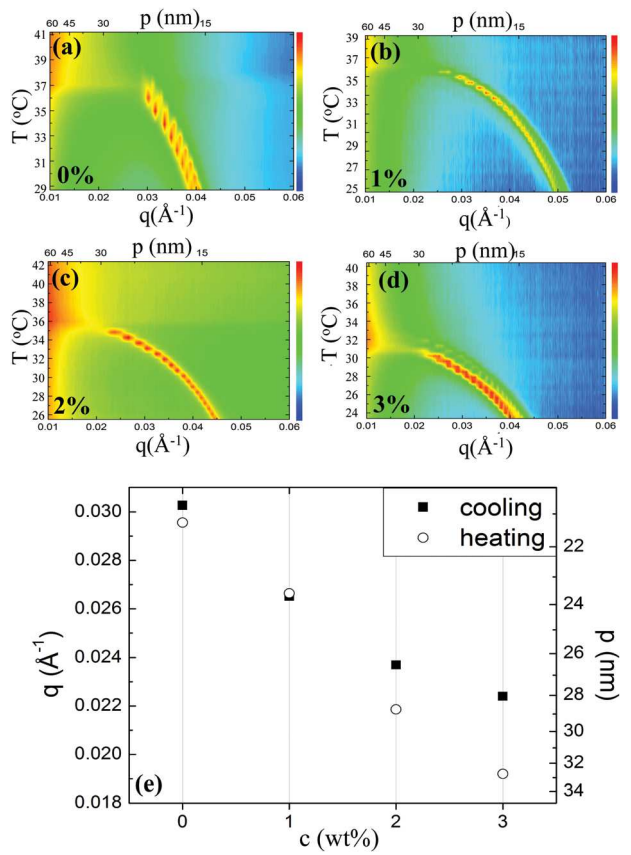

Fig. 3 (a–d) RSoXS intensity *vs.* temperature and scattering wavenumber q (bottom axis) and corresponding spatial periodicity p (top axes) for various chiral additive concentrations. (e) Concentration dependences of the nanoscale periodicity p.

between about 1.5% and 4% ZLI811 concentrations. The bands correspond to areas with helical pitch p being between

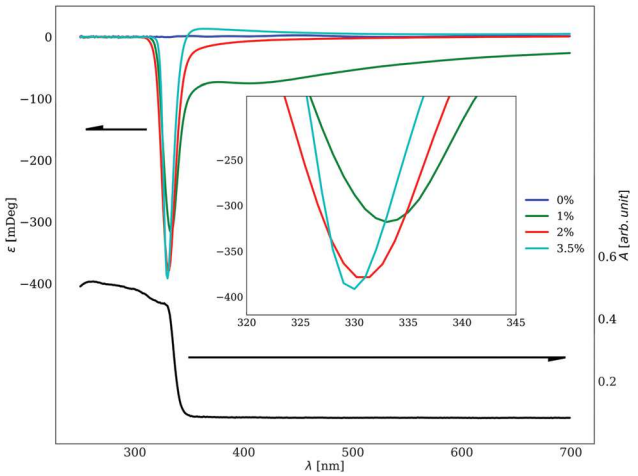

Fig. 4 Left axis: Ellipticity ε (left axis) for neat KA(0.2) and KA(0.2) with 1, 2 and 3.5% ZLI811 additive as a function of wavelength at 68 °C. The inset shows the peak positions for the doped mixtures. Right axis: Wavelength dependence of the absorbance ε for neat KA(0.2).

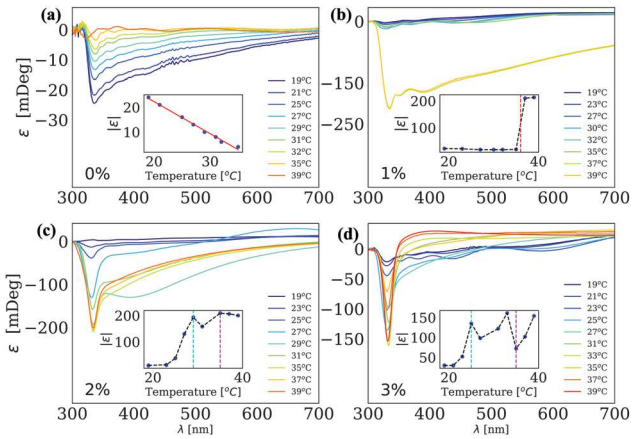

Fig. 5 The wavelength dependences of the ellipticity ε at various temperatures for mixtures with different chiral additive concentrations. (a) 0%; (b) 1%; (c) 2%; (d) 3%. Insets show the temperature dependences of the maximum ellipticities for the corresponding concentrations. The cyan and purple dotted lines indicate boundaries of a new phase below the N* phase.

$p = 2L/(n - 1)$ and $p = 2L/(n + 1)$, where n is an integer, and L = 10 μm is the film thickness. In the middle of the band, the helix is undisturbed with $p = 2L/n$. Combining this with the relation connecting the pitch to concentration c and the helical twisting power (HTP) of the chiral additive: HTP = $1/(p{\cdot}c)$, we get that $n = c{\cdot}2L{\cdot}$HTP. Knowing the film thickness and HTP ~ 10 μm^{-1},[38] the dopant concentration can be estimated with great precision. With this value we obtain n = 8 for c = 4%, *i.e.*, $p \sim 2.5$ μm at 4% ZLI concentration. This value is slightly larger than the number of bands (7) we observe experimentally, and could be explained by the differences between the twist elastic constant K_{22} and the HTP of ZLI811 in KA(0.2) and 5CB.[28] Fig. 1(b) at 34.1 °C shows the appearance of a grainy texture in the band at or above 1.5 wt% ZLI811 concentration, indicating a phase transition; in particular, note the appearance of the

curly defect lines in the image. Fig. 1(c) at 28.7 °C shows a region between about 0.5% and 3 wt% chiral additive concentration with two noteworthy features. First, the boundary between the bands completely disappears below c = 1.5 wt%, and the width of the bands increases above 1.5 wt%. This is consistent with a strong increase in the twist elastic constant, which agrees with the measurements by Adlem *et al.*[28] that show a strong increase in the twist elastic constant just above the transition to the N_{TB} phase. This increase in K_{22} is due to the onset of a pseudolayer structure that is incompatible with the twisted director structure, as noted for another dimer material by Mandle *et al.*[25] Inspection of the textures over a wider concentration range (not shown) revealed that the bands are not fully expelled above 1.5%, indicating the presence of a finite helical pitch that is slightly larger than the pitch in the N* phase. Note that the textures below and above $c \sim 1.5$ wt% are very different: below c = 1.5 wt%, the stripes are parallel to the rubbing direction and resemble elongated focal conics, which are characteristic of the N_{TB} phase. At and above 1.5 wt% concentrations, the stripe structure is much narrower and oriented in the orthogonal direction. This indicates the development of a phase different from the N_{TB} phase. Fig. 1(d) at 24.3 °C shows the concentration range between 1 wt% and 3.5 wt% and reveals the gradual formation of the N_{TB}-type texture, and thus a transition to the N_{TB} phase, even at additive concentrations of 3% and higher for temperatures below 25 °C.

Phi-Viz imaging of a L = 4.7 μm thick film of KA(0.2) + 2% ZLI811 maps the direction of the average optic axis and the average retardance as displayed in Fig. 2. The dark lines indicate directions perpendicular to the optic axis at the top of the film. Fig. 2(a) for temperature T = 35.0 °C (N* phase) shows a uniform texture with an optic axis parallel to the rubbing direction. The retardance is low due to the orientation of the helix normal to the substrates. In Fig. 2(b) for T = 33 °C, a domain texture with differently oriented parallel stripes is observed. Comparing this with Fig. 1(b), we judge that the new texture represents the lower range of the N* phase, where the elastic constants increase on cooling. Less than 1 degree below this point, another uniform texture forms, as shown in Fig. 2(c) for T = 32.0 °C. In contrast to the uniform texture in Fig. 2(a), here the optical axis at the top of the film makes an angle of 33° with the rubbing direction. This average optic axis rotates by more than 100°, and the average retardance increases by about 70 nm on further cooling by ~0.5 °C. Starting at around T = 31.4 °C, stripes form along the rubbing direction resembling the optical stripes of the N_{TB} phase. The average retardation increases to 160 nm, consistent with the elimination of the helical structure (whose axis was originally along the substrate normal). On further cooling to 25 °C, the average retardance gradually decreases to 140 nm.

Fig. S3–S5 in the ESI† show typical POM textures of the 5 μm films in cells with planar alignment treatment and for uniform additive concentrations of 1, 2.5 and 3.5 wt%. While the 1% mixture shows only a direct transition from a uniform (N*) texture to a striped texture with stripes along the rubbing direction, corresponding to the N_{TB}-phase, the 2.5% and 3.5% mixtures first transition (at 32.5 °C and 31.0 °C, respectively) from the planar N* state to a state characterized by an inhomogeneous texture with randomly shaped defect loops. The stripes parallel to the rubbing direction appear gradually at lower temperatures (28 °C and 25 °C for 2.5 and 3.5 wt% mixtures, respectively). These observations support our POM results in contact cells (see Fig. 1), which indicate the formation of an intermediate phase between the N* and N_{TB}* phases for $c \geq 1.5$ wt%.

The temperature dependences of the RSoXS intensities in the 0.01–0.06 $Å^{-1}$ q range (left axes) and 60–10 nm pitch range (right axes) are shown for c = 0, 1, 2 and 3 wt% ZLI811 concentrations in Fig. 3(a–d). The concentration dependences of the positions of the maximum intensities at the highest temperatures, where diffraction peaks appear, are shown in Fig. 3(e). The most striking feature of these results is that the nanoscale periodicity associated with the twist-bend heliconical structure is increasing upon the addition of the chiral additive from about 20 nm at c = 0% to 30 nm at 3 wt%.

Another noteworthy feature of the RSoXS results is the increase in the peak width for the 3% mixture (Fig. 3(d)). This behavior can be seen in more detail in Fig. S6 (ESI†), where we compare the q-dependencies of the scattering intensities for the 2 wt% and 3 wt% mixtures at various temperatures.

Circular dichroism (CD) is a well-established chiroptical technique which can quantify enantiomeric excess (e.e.) associated with a chiral molecule.[39,40] Induced circular dichroism (iCD) measurements, however, detect chirality induced by chiral additives *via* recording the linear dichroism spectra of the host species, which are then averaged to cancel linear dichroism and birefringence in the particular case of the LC phases.[41,42]

Fig. 4 shows the ellipticity ε (left axis) for neat KA(0.2) and KA(0.2) with 1, 2 and 3.5% ZLI811 concentrations as a function of wavelength in the N* phase at 68 °C. As expected, in the N phase there is no CD signal for neat KA(0.2). The iCD signal increases with increasing concentration of the chiral additive from 1 to 3.5 wt%. The increase is not linear, as the I–N* transition temperature decreases with increasing additive concentration, so the distance from the clearing point (therefore the order parameter) decreases from 4 °C of 1 wt% to 1 °C of 3.5 wt% concentration mixture (see Fig. S2, ESI†). For all concentrations, the iCD signals have maxima between 330 nm and 335 nm. This is at the edge of the absorption of KA(0.2), as plotted at the bottom of Fig. 4 (against the right axis). The absorption below 330 nm is due to the presence of the benzene rings and is typical for liquid crystal materials. Peaks become sharper with increasing wt% of chiral additive and slightly shift to shorter wavelengths.

The iCD signals at different temperatures through the N–N_{TB} range are shown in Fig. 5. Insets show the temperature dependences of the peak positions.

Fig. 5(a–d) show the wavelength dependencies of the ellipticities ε at various temperatures for mixtures with different chiral additive concentrations ranging from 0 to 3%. It is remarkable that the N_{TB} phase of the neat KA(0.2) (see Fig. 5(a)) exhibits an increasing ellipticity on cooling with maxima at around 330 nm. As shown in the inset to Fig. 5(a), the maximum ellipticity is linearly increasing from zero at the N–N_{TB} transition to 23 at 18 °C below the transition.

The temperature dependences of ε for the samples with the chiral additives (Fig. 5(b–d)) are quite different. The simplest behavior is observed in the 1% mixture, where the ellipticity drops from about 200 to 10 within one degree at 37 °C, and then the signal linearly increases to about 20 at 18 °C. The temperature behavior of the maximum intensities becomes non-monotonic for the 2% and 3% samples, in which the POM and Phi-Viz observations suggested an intermediate phase between the N* and N_{TB}* phases. In accordance with this, the temperature dependences of the iCD signals show local minima in the temperature range comparable to the intermediate phase indicated by the optical measurements. Below this intermediate range, the iCD signals drop quickly upon the transition to the N_{TB}* phase.

A phase diagram from a few degrees above the N–N_{TB} transition of the neat KA(0.2) down to room temperature is assembled by combining information of RSoXS, POM, PolaViz and iCD measurements as shown in Fig. 6.

On cooling from the uniform texture of the N* phase with planar anchoring, at a roughly constant temperature corresponding to the N–N_{TB} transition of the neat KA(0.2) (37 °C), modulated textures with various patterns shown in Fig. S3–S6 (ESI†) appear presumably due to the strongly varying helical pitch. On further cooling, this state is terminated by a front of uniform texture. The concentration dependence of the temperature at the front with uniform texture appears to coincide with that of the appearance of the Bragg reflection seen by RSoXS showing that this state has a pseudo layered nanostructure, *i.e.*, it is not an N* phase anymore. POM and PolaViz textures show a formation of optical stripes about 1–2 degrees below this transition. As explained by Challa *et al.*,[43] these stripes are due to the decreasing periodicity of the pseudo layers. The range between the appearance of the front of uniform texture and the formation of the optical stripes is shaded by darker blue.

Importantly, in this range, the iCD signals are still comparable with that in the N* phase and they start dropping to zero only 2–3 °C below. The range between the two maxima of the iCD signals is shaded by light blue. Importantly, the upper limit of this range coincides with the range where the front and the nanoscale periodicity appear.

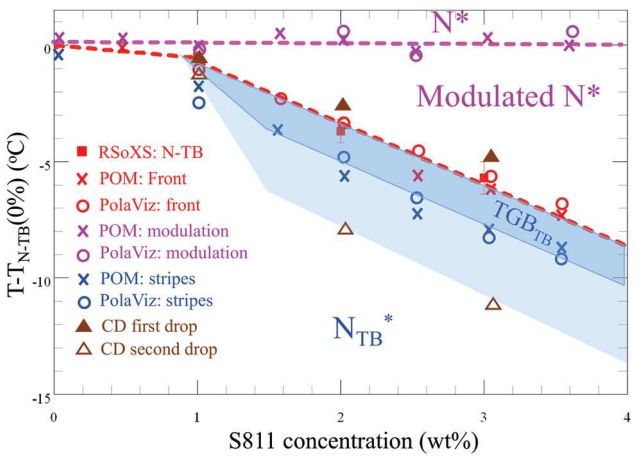

Fig. 6 The phase diagram of a chiral additive in the N_{TB} system at a temperature relative to the N–N_{TB} transition of the neat KA(0.2), which is 37 °C.

D. Discussion

One of the most striking effects of the chiral additive on the N_{TB} structure is the 50% increase in the nanoscale pitch at only 3% ZLI811 concentration. This is in stark contrast to prior observation on CB7CB mixed with pentyl cyano-biphenyl (5CB), where 37% of 5CB caused only a 20% increase in the nanoscale pitch.[44] In that system, most of the 5CB molecules were shown to be expelled from the individual helicons, explaining why they only slightly influenced the heliconical structure. The fact that the specific extension $(\Delta p/p)/c$ is more than 30 times larger in our system, indicates that the ZLI811 molecules are largely incorporated into the helical chain structure. Since ZLI811 is rod-like, the average curvature radius of the molecules R_{mol} increases. The heliconical pitch p_H at the onset of the RSoXS signal is determined by R_{mol} as $p_H = 2\pi R_{mol}$;[44] thus the p_H increases proportionally to R_{mol}. We propose that this mechanism and the decreased packing order explain the large increase of the p_H upon the addition of a small amount of ZLI811. According to this model, the major difference between 5CB and ZLI811 is the molecular flexibility and not the chirality; the ester unit between the benzene rings in ZLI811 (see Fig. S1, ESI†) makes it more flexible than 5CB, which has a rigid biphenyl in its core.

The other significant result of our studies described above is the appearance of the intermediate phase between the N* and the N_{TB}* phase at $c > 1.5$ wt% ZLI811 concentrations. The coincidence of the front of the uniform texture and the appearance of the RSoXS signals seen in Fig. 6 shows that this phase has a nanoscale periodicity, such as the N_{TB} phase, and has an iCD signal comparable to that in the N* phase, indicating the helical arrangements of the benzene rings of neighbor molecules normal to the substrates, such as in the N* phase. To understand the consequences of these two observations on the structure of this intermediate phase, we will need to understand the possible mechanisms for the molecular chirality transfers for the N* and N_{TB}* phases, as sketched in Fig. 7.

In the N* phase, the director rotates along the helix axis $\hat{h}$ and is normal to it (see Fig. 7(a)), just as known for the rod-shape monomeric molecules. This helix represents twisting of the neighboring benzene rings with respect to each other along the helical axis, which is normal to the film substrates. This rotation leads to the iCD signals at around 330 nm (see Fig. 4).

In the N_{TB} phase, the director is constrained to rotate on a cone of the nanoscale (p_H = 10–30 nm) helix with helicone axis $\hat{c}$ (see Fig. 7(b)). Biasing this rotation by the chiral additive may modulate the nanoscale pitch by increasing the pitch for one sign of the helix sense, and by decreasing it for the other sign (see Fig. 7(b)). This would lead to a splitting of the RSoXS signal, which we observe for the 3% concentration (see Fig. 3(d) and Fig. S6, ESI†). Such a chirality transfer is different from the twisting of the neighboring biphenyls along the normal film

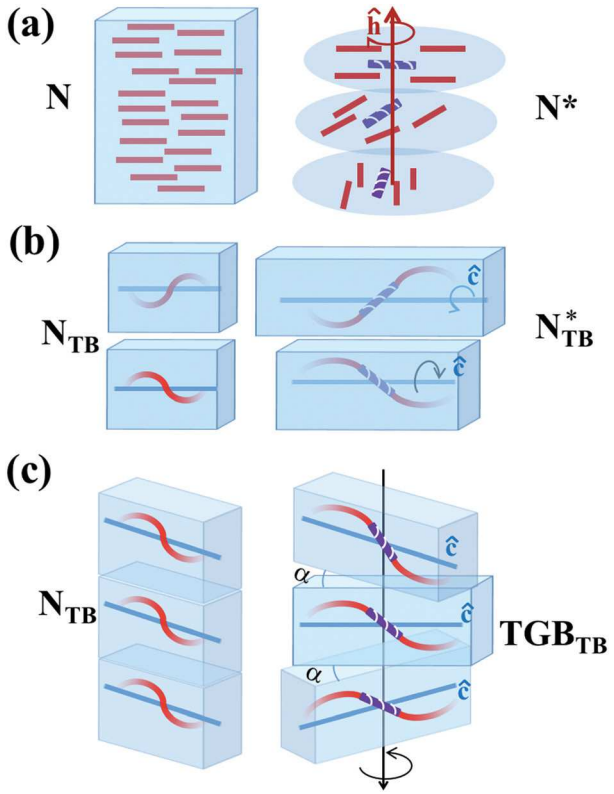

Fig. 7 The schematic illustration of chirality transfers due to the chiral additives (a purple rod with white grooves to illustrate the molecular chirality) in the N and N_{TB} phase. (a) The chiral additives in the N phase leads to N* (or the cholesteric phase), whereby the director rotates helically around an axis perpendicular to the director. (b) In the N_{TB} phase, the molecular chirality may modulate the nanoscale pitch, or (c) it can break the pseudo layers into blocks that rotate with respect to each other (TGB_{TB}).

and would not lead to an iCD signal at around 330 nm. Indeed, we see some modulations of the CD signals above 400 nm. They may be related to the micron-scale stripe textures, but their full understanding would require further studies on more dimer materials, which are out of the scope of this paper.

The iCD signals of the mixture with 1 wt% ZLI811 concentration (see Fig. 5(b)), where no intermediate phase was observed shows a sharp decrease in the iCD signal upon the direct N*–N_{TB}* transition, confirming that the effect of the molecular chirality on the N_{TB}* is very weak. However, at above 1.5 wt% chiral additive concentrations, the iCD signals at 330 nm are comparable to that in the N* state, showing similar twist among the biphenyls as in N*. That is only compatible with the pseudo layer structure if the pseudo layers twist with respect to each other. In strongly chiral layered smectic A materials, the smectic layers break into small blocks that twist with respect to each other across the grain boundaries. Such a phase is called the twist grain boundary (TGB_A) phase[45–48] and usually forms in a narrow range below the N* phase.

In the N_{TB} phase, the compressibility of the pseudo layers is about 3 orders of magnitude smaller than the smectics.[49] This phase (which we will call TGB_{TB} to emphasize the analogy with the layered TGB_A phase), may form even at lower chirality and in wider temperature ranges than the TGB_A phase. The proposed structure of TGB_{TB}, where the adjacent blocks of pseudo-layers rotate across the grain boundaries, which are composed of lattices of the pseudo-layer screw dislocations, is sketched in Fig. 7(c). The temperature range of the TGB_{TB} phase of the studied chiral KA(0.2) mixtures is indicated with light blue shading in Fig. 6.

Note that in the direction along the light and at the visible wavelength range, the TGB-like structure also means a successive rotation of the benzene rings (see right-hand side sketches of Fig. 7(a and c)), thus explaining the maximum of the signals at around 330 nm. We also note that the existence of a TGB_{TB}-type structure, where the TB nematic pseudo-layers are accompanied by a secondary twist along an orthogonal axis (parallel to the pseudo-layer planes), has been proposed theoretically.[50,51]

Finally, the increase in the ellipticity on cooling in the N_{TB} phase (without chiral additive) is quite striking. Since the dimensions of the illuminated area ($\sim$20 mm^2) used in the CD measurements are much larger than the typical width of stripes with uniform chirality (about twice the film thickness of $\sim$14 μm),[18] we would expect the ellipticity of a uniform domain to be about 5 mm/14 μm $\sim$ 350 times larger than the value (up to 23) we measured. Accordingly, it could be as high as eight thousand, which is about 20 times larger than the measured maximum ellipticity in the N* phase (Fig. 4(c)). This is related to the much smaller heliconical pitch p_H of the N_{TB} phase compared to the N*, where $P \sim 2$ μm for the 3% mixture. The $P/p_H \sim 2$ μm/30 nm $\sim$ 70 is about 3 times larger than the estimated 20-fold increase. This could be due to the nature of the rough estimate, and/or may indicate that the CD signal scales with the heliconical angle. Clearly, this issue deserves further study utilizing a larger number of N_{TB} host materials. Such measurements are in progress.

E. Conclusions

In this manuscript, we studied the rare case when ambidextrous chirality with nanoscale pitch due to spontaneous symmetry breaking is influenced by the molecular chirality of chiral additives. We have shown that the ambidextrous nanoscale pitch of the N_{TB} phase increases and the chiral transfer among the biphenyl groups disappears in the N_{TB}* phase. Most significantly, our observations indicate the appearance of a TGB-type phase at $c > 1.5$ wt% chiral additive concentrations below the usual N* phase and above the non-CD active N_{TB}* phase. Such a TGB/twist-bend hybrid should spur more theoretical and experimental studies. For example, a TGB_{TB} phase should have a distinct DLS signature – namely, a gap in the wavenumber dependence of the pseudo-layer undulation mode at $q = 0$ Å^{-1},[52] which arises due to the rotation of the pseudo-layer blocks and thus of the heliconical axis. Finally, we speculate that one of the phases of the chiral dimers reported by Gorecka *et al.*,[22,23] which exhibits an unusually long pitch of $\sim$60 nm, might actually have the TGB_{TB} structure.

Contributions

MM, MS, AN, CB, ZS, HR, TV, and SMS did measurements. VN, CZ, AI, and SMS designed the experimental instruments.

TH directed the iCD measurements and analysed the data. SNS and JG analysed the data. AJ directed the measurements and analyzed the data. MM, MS, TH, SNS, JG and AJ wrote the paper.

Conflicts of interest

There are no conflicts to declare.

Acknowledgements

This work was supported by the U.S. National Science Foundation (NSF) DMR-1506018 and DMR 1307674 and NSF REU CHE-1659571. The beamline 11.0.1.2 at the Advanced Light Source at the Lawrence Berkeley National Laboratory is supported by the Director of the Office of Science, Office of Basic Energy Sciences, of the U.S. Department of Energy under Contract No. DE-AC02-05CH11231.

References

1 T. Sekine, T. Niori, J. Watanabe, T. Furukawa, S.-W. Choi and H. Takezoe, *J. Mater. Chem.*, 1997, **7**, 1307–1309.
2 D. R. Link, G. Natale, R. Shao, J. E. Maclennan, N. A. Clark, E. Körblova and D. M. Walba, *Science*, 1997, **278**, 1924–1927.
3 A. Eremin and A. Jákli, *Soft Matter*, 2013, **9**, 615–637.
4 M. Nagaraj, *Liq. Cryst.*, 2016, **43**, 2244–2253.
5 L. E. Hough, M. Spannuth, M. Nakata, D. A. Coleman, C. D. Jones, G. Dantlgraber, C. Tschierske, J. Watanabe, E. Körblova, D. M. Walba, J. E. Maclennan, M. A. Glaser and N. A. Clark, *Science*, 2009, **325**, 452–456.
6 L. E. Hough, H. T. Jung, D. Krueerke, M. S. Heberling, M. Nakata, C. D. Jones, D. Chen, D. R. Link, J. A. N. Zasadzinski, G. Heppke, J. P. Rabe, W. Stocker, E. Koerblova, D. M. Walba, M. A. Glaser and N. A. Clark, *Science*, 2009, **325**, 456–460.
7 C. Zhang, N. Diorio, O. D. Lavrentovich and A. Jákli, *Nat. Commun.*, 2014, **5**, 3302.
8 L. Li, M. Salamonczyk, A. Jákli and T. Hegmann, *Small*, 2016, **12**, 3944–3955.
9 L. Li, M. Salamończyk, S. Shadpour, C. Zhu, A. Jákli and T. Hegmann, *Nat. Commun.*, 2018, **9**, 3–10.
10 I. Dozov, *Europhys. Lett.*, 2001, **56**, 247–253.
11 M. Cestari, S. Diez-Berart, D. A. Dunmur, A. Ferrarini, M. R. De La Fuente, D. J. B. Jackson, D. O. Lopez, G. R. Luckhurst, M. A. Perez-Jubindo, R. M. Richardson, J. Salud, B. A. Timimi and H. Zimmermann, *Phys. Rev. E: Stat., Nonlinear, Soft Matter Phys.*, 2011, **84**, 031704.
12 P. A. Henderson and C. T. Imrie, *Liq. Cryst.*, 2011, **38**, 1407–1414.
13 V. P. Panov, R. Balachandran, M. Nagaraj, J. K. Vij, M. G. Tamba, A. Kohlmeier and G. H. Mehl, *Appl. Phys. Lett.*, 2011, **99**, 261903.
14 L. Beguin, J. W. Emsley, M. Lelli, A. Lesage, G. R. Luckhurst, B. A. Timimi and H. Zimmermann, *J. Phys. Chem. B*, 2012, **116**, 7940–7951.
15 C. Zhu, C. Wang, A. Young, F. Liu, I. Gunkel, D. Chen, D. M. Walba, J. E. Maclennan, N. A. Clark and A. Hexemer, *Nano Lett.*, 2015, **15**, 3420.
16 C. Zhu, M. R. Tuchband, A. Young, M. Shuai, A. Scabrough, D. M. Walba, J. E. Maclennan, C. Wang, A. Hexemer and N. A. Clark, *Phys. Rev. Lett.*, 2016, **116**, 147803.
17 V. Borshch, Y.-K. Kim, J. Xiang, M. Gao, A. Jakli, V. P. Panov, J. K. Vij, C. T. Imrie, M. G. Tamba, G. H. Mehl and O. D. Lavrentovich, *Nat. Commun.*, 2013, **4**, 2635.
18 C. Meyer, G. R. Luckhurst and I. Dozov, *Phys. Rev. Lett.*, 2013, **111**, 067801.
19 R. R. Ribeiro de Almeida, C. Zhang, O. Parri, S. N. Sprunt and A. Jákli, *Liq. Cryst.*, 2014, **41**, 1661–1667.
20 D. Chen, J. H. Porada, J. B. Hooper, A. Klittnick, Y. Shen, M. R. Tuchband, E. Korblova, D. Bedrov, D. M. Walba, M. A. Glaser, J. E. Maclennan and N. A. Clark, *Proc. Natl. Acad. Sci. U. S. A.*, 2013, **110**, 15931–15936.
21 M. Salamończyk, N. Vaupotič, D. Pociecha, C. Wang, C. Zhu and E. Gorecka, *Soft Matter*, 2017, **13**, 6694–6699.
22 A. Zep, S. Aya, K. Aihara, K. Ema, D. Pociecha, K. Madrak, P. Bernatowicz, H. Takezoe and E. Gorecka, *J. Mater. Chem. C*, 2013, **1**, 46.
23 E. Gorecka, N. Vaupotič, A. Zep, D. Pociecha, J. Yoshioka, J. Yamamoto and H. Takezoe, *Angew. Chem.*, 2015, **54**, 10155–10159.
24 R. Balachandran, V. P. Panov, Y. P. Panarin, J. K. Vij, M. G. Tamba, G. H. Mehl and J. K. Song, *J. Mater. Chem. C*, 2014, **2**, 8179–8184.
25 R. J. Mandle, E. J. Davis, C. T. Archbold, S. J. Cowling and J. W. Goodby, *J. Mater. Chem. C*, 2014, **2**, 556–566.
26 C. T. Archbold, E. J. Davis, R. J. Mandle, S. J. Cowling and J. W. Goodby, *Soft Matter*, 2015, **11**, 7547.
27 S. M. Salili, R. R. Ribeiro de Almeida, P. K. Challa, S. N. Sprunt, J. T. Gleeson and A. Jakli, *Liq. Cryst.*, 2017, **44**, 160–164.
28 K. Adlem, M. Čopič, G. R. Luckhurst, A. Mertelj, O. Parri, R. M. Richardson, B. D. Snow, B. A. Timimi, R. P. Tuffin and D. Wilkes, *Phys. Rev. E: Stat., Nonlinear, Soft Matter Phys.*, 2013, **88**, 022503.
29 R. B. Meyer, *Appl. Phys. Lett.*, 1968, **12**, 281–282.
30 P. G. De Gennes, *Solid State Commun.*, 1968, **6**, 163–165.
31 J. Xiang, S. V. Shiyanovskii, C. Imrie and O. D. Lavrentovich, *Phys. Rev. Lett.*, 2014, **112**, 217801.
32 J. Xiang, Y. Li, Q. Li, D. A. Paterson, J. M. D. Storey, C. T. Imrie and O. D. Lavrentovich, *Adv. Mater.*, 2015, **27**, 3014–3018.
33 J. Xiang, A. Varanytsia, F. Minkowski, D. A. Paterson, J. M. D. Storey, C. T. Imrie, O. D. Lavrentovich and P. Palffy-Muhoray, *Proc. Natl. Acad. Sci. U. S. A.*, 2016, **113**, 12925–12928.
34 S. M. Salili, J. Xiang, H. Wang, Q. Li, D. A. Paterson, C. T. Imrie, O. D. Lavrentovich, S. N. Sprunt, J. T. Gleeson and A. Jakli, *Phys. Rev. E*, 2016, **94**, 042705.
35 L. Longa and G. Pająk, *Phys. Rev. E*, 2016, **93**, 040701(R).
36 R. J. Mandle and J. W. Goodby, *Soft Matter*, 2018, **14**, 8846–8852.
37 H. Qi, J. O'Neil and T. Hegmann, *J. Mater. Chem.*, 2008, **18**, 374–380.
38 S.-W. Ko, S.-H. Huang, A. Y.-G. Fuh and T.-H. Lin, *Opt. Express*, 2009, **17**, 15926–15931.
39 L. Chen, Y. Zhao, F. Gao and M. Garland, *Appl. Spectrosc.*, 2003, **57**, 797–804.

40 S. Barman and E. V. Anslyn, *Tetrahedron*, 2014, **70**, 1357–1362.
41 A. Sharma, T. Mori, H. C. Lee, M. Worden, E. Bidwell and T. Hegmann, *ACS Nano*, 2014, **8**, 11966–11976.
42 A. Nemati, S. Shadpour, L. Querciagrossa, L. Li, T. Mori, M. Gao, C. Zannoni and T. Hegmann, *Nat. Commun.*, 2018, **9**, 1–13.
43 P. K. Challa, V. Borshch, O. Parri, S. N. Sprunt, C. T. Imrie, S. N. Sprunt, J. T. Gleeson, O. D. Lavrentovich and A. Jákli, *Phys. Rev. E: Stat., Nonlinear, Soft Matter Phys.*, 2014, **89**, 060501(R).
44 M. R. Tuchband, M. Shuai, K. A. Graber, D. Chen, C. Zhu, L. Radzihovsky, A. Klittnick, L. Foley, A. Scarbrough, J. H. Porada, M. Moran, J. Yelk, E. Korblova, D. M. Walba, A. Hexemer, J. E. Maclennan, A. Matthew and N. A. Clark, 2017, arXiv:1703.10787v1.
45 P.-G. de Gennes, *The Physics of Liquid Crystals*, Clarendon Press, Oxford, 2nd edn, 1974, ch. 7.
46 S. R. Renn and T. C. Lubensky, *Phys. Rev. A: At., Mol., Opt. Phys.*, 1988, **38**, 2132–2147.
47 J. W. Goodby, M. A. Waugh, S. M. Stein, E. Chin, R. Pindak and J. S. Patel, *Nature*, 1989, **337**, 449–452.
48 H.-S. Kitzerow, A. J. Slaney and J. W. Goodby, *Ferroelectrics*, 1996, **179**, 61–80.
49 S. M. Salili, C. Kim, S. Sprunt, J. T. Gleeson, O. Parri and A. Jákli, *RSC Adv.*, 2014, **4**, 57419–57423.
50 C. Meyer and I. Dozov, *Soft Matter*, 2016, **12**, 574–580.
51 I. Dozov and C. Meyer, *Liq. Cryst.*, 2017, **44**, 4–23.
52 T. C. T. C. Lubensky, *Phys. Rev. A: At., Mol., Opt. Phys.*, 1972, **6**, 452–470.

